Références

BELAKHOVSKY, M. & PIERRE, J. (1971). *Solid State Commun.* **9**, 1409.
BERTAUT, E. F. (1958). *C.R. Acad. Sci. Paris*, **246**, 3335.
HASTINGS, J. M., CORLISS, L. M., BLUME, M. & PASTERNAK, M. (1970). *Phys. Rev.* **B1**, 3209.
KEFFER, F. (1962). *Phys. Rev.* **126**, 896.
KEFFER, F. & O'SULLIVAN, W. (1957). *Phys. Rev.* **108**, 637.
KOUVEL, J. S. & KASPER, J. S. (1963). *J. Phys. Chem. Solids*, **24**, 529.
LI, Y. Y. (1955). *Phys. Rev.* **100**, 627.
ROTH, W. L. (1958). *Phys. Rev.* **111**, 772.
SHIRANE, G. (1959). *Acta Cryst.* **12**, 282.
UMEBAYASHI, H. & ISHIKAWA, Y. (1966). *J. Phys. Soc. Japan*, **21**, 1281.
WINTENBERGER, M., CHAMARD-BOIS, R., BELAKHOVSKY, M. & PIERRE, J. (1971). *Phys. Stat. Sol.* (*b*) **48**, 705.

Acta Cryst. (1972). A**28**, 344

Crystal Surface Morphology Developed During the Sublimation of Oriented Zinc Single Crystals

BY G. M. ARNSTEIN,* P. BOLSAITIS AND R. W. ARMSTRONG

Engineering Materials Group, University of Maryland, College Park, Maryland 20740, *U.S.A.*

(*Received* 17 *August* 1970)

The surface structure of zinc single crystals subjected to a sublimation treatment has been studied by the techniques of optical metallography, optical goniometry and by Laue X-ray diffraction. Right cylinders with a $\langle 001 \rangle$ axis were enclosed, with titanium getter material, in Vycor tubes evacuated to 10^{-5} mm Hg and heated to temperatures in the vicinity of 370°C for periods of 100 to 200 hr. A thermal gradient existed in the evacuated chamber such that zinc was transported from one end of the tube to the other end. The sublimation process exposed macroscopically visible crystallographic planes in local regions of the crystals. The three-dimensional structure of the facet morphology has been determined. The exposed planes are of the type $\{10\overline{1}0\}$, $\{40\overline{4}1\}$, $\{30\overline{3}1\}$, $\{30\overline{3}2\}$, $\{10\overline{1}1\}$, $\{40\overline{4}5\}$, $\{20\overline{2}3\}$ and $\{10\overline{1}\,10\}$. The $\{0001\}$ surfaces were relatively unaffected by the sublimation process. The facet structures appear to be related to some extent to the dislocation substructure and also to the Gibbs–Wulff surface energy construction for zinc.

Introduction

In contrast to extensive studies on the sublimation properties of cubic metals (Moore, 1963) little research has been done to investigate this phenomenon for hexagonal close-packed crystals. Andrade & Randall (1950) observed surface pitting which was produced by the thermal etching of cadmium single crystals having surfaces cut near $\{0001\}$. They concluded that the $\{0001\}$ basal plane was thermally the most stable crystal plane, followed next in stability by the first order pyramidal planes of type $\{10\overline{1}1\}$. Miller, Carpenter & Chadwick (1969) have recently attributed the appearance of polygonal bubbles which were observed in thin films of zinc, following argon-ion bombardment, to the anisotropy of the crystal surface free energy, thus concluding that the internal bubbles were conforming to a proposed equilibrium (Gibbs–Wulff) shape composed of $\{0001\}$, $\{10\overline{1}1\}$ and $\{10\overline{1}0\}$ surfaces (*cf.* Gibbs, 1961; Wulff, 1901). The same crystallographic results have been observed for cadmium and magnesium by Kirchner & Chadwick (1969).

* Fellow of the Council of Scientific and Humanistic Development of the Central University of Venezuela (UCV).

The principal result of these preceding investigations is to provide support for the notion that the anisotropy of the surface free energy is responsible for the specific crystallographic appearance of the surface structures which are produced. This result should reasonably be expected to apply for the small polygonal shapes observed in thin films because the contribution of the specific surface energy, γ_{ij}, to an experimental change in surface area, A_j, should give an energy change comparable to the volume dependent energy change (Herring, 1951). However, the same result might also be expected to apply for large scale crystallographically faceted structures such as those described by Andrade & Randall, if it were presumed that these large structures are simply geometrically similar to the multitudinous submicroscopic structures of which they are composed. On this basis, we chose to investigate the sublimation structures which might be produced in bulk single crystals subjected to heat treatment in a thermal gradient whereby appreciable sublimation of zinc atoms would occur. The possibility of observing significant crystallographic features in the partially sublimed crystals was expected to be enhanced because the maximum ratio of surface energies for zinc is $(\gamma\{1\overline{2}10\}/\gamma\{0001\}) \simeq 2{\cdot}2$ as compared, for example, with maximum ratio values < 1·1 for cubic metals (Moore, 1958; Drechsler & Nicholas, 1967).

Experimental details

The zinc crystals were produced as right cylindrical rods of 8 mm diameter and about 10 cm long with their axes parallel to ⟨0001⟩ (Schultz & Armstrong, 1964). The specified purity of the starting material was 99·9999 %, whereas a complete analysis following the growth of the crystal proved them to be of 99·9 % purity, the major contaminants being nonmetallic impurities such as hydrogen and nitrogen (Schultz & Armstrong, 1964).

Specimens for the sublimation treatment were produced from the initial crystal rods by cleaving them at liquid nitrogen temperature to produce samples of approximately 7 mm height. A number of Laue back reflection pictures were taken to check the initial orientation of the crystals and to obtain a qualitative indication of their perfection preceding the sublimation treatment.

Subsequently the single crystals were enclosed, as shown in Fig. 1, in Vycor tubes that were evacuated to 10^{-5} mm Hg and contained 99·999 % pure titanium sheet cuttings which were used as a getter to reduce the partial pressure of oxygen in the capsule (Darken & Gurry, 1953). This sealed Vycor assembly was hung inside a quartz tube furnace chamber having the thermal environment which is also shown in Fig. 1. The samples were always placed at the rather level peak temperature of the profile of the furnace (axial gradient of $\sim 1\,°C.cm^{-1}$) to insure that the vapor produced in the sublimation process condensed in the cooler zone of the capsule, far from the specimen. The samples were heated for time periods ranging from 100 to 200 hr.

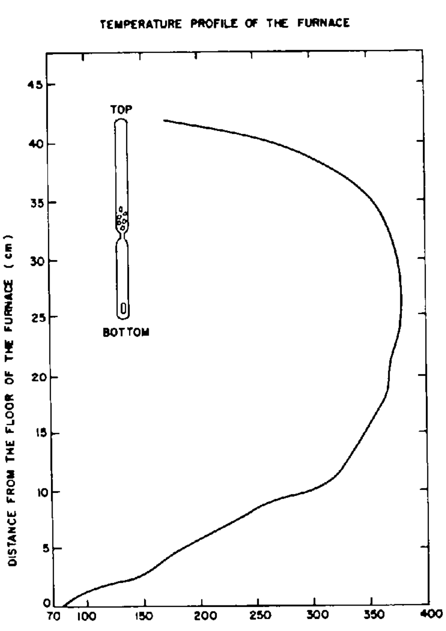

Fig. 1. Temperature profile of the furnace and location of the specimen.

Following the sublimation treatments, the crystals were removed for observation and structural analysis by optical metallography, X-ray diffraction and optical goniometry. Fig. 2 (*a*) and (*b*) shows two views of one such crystal. The {0001} cleavage surface was unchanged in all cases by the sublimation treatment and this surface was employed, therefore, as the reference surface for each type of measurement. Several micrographs were taken of particular crystallographic features with an Ultrascan electron scanning microscope.

Results

It is evident in Fig. 2 (*a*) and (*b*) that the sublimation treatments were sufficiently extensive to produce polygonal holes which could be visually observed at various positions on the cylindrical surfaces of the crystals (where appreciable sublimation had occurred). The overall crystal dimensions were otherwise not significantly altered during the sublimation treatment.

An examination of these various local regions showed that essentially two types of polygonal holes were present, as shown schematically in Fig. 3 (*a*) and (*b*). The holes appeared to be randomly distributed around the cylindrical crystal surfaces. In one case, a crystal exhibited an exceptional amount of sublimation from the top circumferential edge of the cylinder and this led to a remnant {0001} plateau of height equal to $\sim\frac{1}{2}$ the original crystal length surrounded by microscopically faceted walls of nearly cylindrical, macroscopic symmetry.

As a first step towards identifying the crystallographic nature of the polygonal holes, Laue back reflection pictures were taken at these sites with the X-ray beam always perpendicular to ⟨0001⟩. At least two pictures were taken in each case: one with the beam perpendicular to a prominent striated surface and one with the beam perpendicular to the boundary which was formed at the intersection of two striated surfaces. The results showed that the striated surfaces contained planes having $\langle 1\bar{2}10\rangle$ zone axes and that the boundaries between the striated surfaces appeared to be in planes also containing $\langle 1\bar{2}10\rangle$ axes. These measurements were found to be consistent with the measurements of surface reflections by optical goniometry. Table 1 shows that plane reflections were generally found showing sixfold rotational symmetry orthogonal to the ⟨0001⟩ axis, as expected for planes of type $\{10\bar{1}0\}$. However, it should be appreciated that the optical goniometric measurements were not in themselves sufficient to determine that the $\{10\bar{1}0\}$ were being exposed because the $\{1\bar{2}10\}$ also show sixfold rotational symmetry about ⟨0001⟩. Next, specific measurements were made of the angular positions around the various $\langle 1\bar{2}10\rangle$ axes at which specular reflections could be observed with the optical goniometer. Table 2 presents the results of a number of the measurements in comparison with calculated angles between particular planes. From data of the type given in these tables and other particular observations which were made during the measurements, the following conclusions are reported:

1. The planes exposed during the sublimation are definitely of type $\{10\bar{1}0\}$, $\{10\bar{1}1\}$, $\{20\bar{2}3\}$ and $\{40\bar{4}1\}$; and, possibly additional plane surfaces of type $\{20\bar{2}1\}$, $\{30\bar{3}1\}$, $\{30\bar{3}2\}$, $\{40\bar{4}5\}$ and $\{10\bar{1}10\}$ are exposed.
2. The $\{10\bar{1}1\}$, $\{20\bar{2}3\}$ and $\{40\bar{4}1\}$ planes appear most frequently in the polygonal holes.
3. The $\{10\bar{1}0\}$ surfaces appear relatively few times but they encompass a large area of several of the holes.
4. The uncertainty in specifying some of the planes in Table 2 is principally due to the substructure misorientations within the crystals, which is of the order of 2° as determined by X-ray diffraction.
5. The $\{10\bar{1}\,10\}$ reflection was observed to show the greatest specularity.

Table 1. *Reflections around the* $\langle 0001\rangle$ *axis of zinc single crystals after partial sublimation*

Number of reflection	1	2	3	4	5	6
Measured angle	58°38′	58°24′	58°	62°	60°18′	62°40′

Table 2. *Angles between the normal to the basal surface and the normals to the planes developed in striated surfaces of the polygonal holes*

Identified plane	Measured angle (with respect to $\{0001\}$)	Number of measurements
$\{10\bar{1}\,10\}$	11°30′	1
$\{20\bar{2}3\}$	$55\pm2°$	12
$\{20\bar{2}3\}$	$55\pm3°$	5
$\{40\bar{4}5\}$	$60\pm1°$	9
$\{10\bar{1}1\}$	$65\pm1°$	10
$\{10\bar{1}1\}$	$65\pm3°$	7
$\{30\bar{3}2\}$ or $\{40\bar{4}3\}$	70°58′	1
$\{30\bar{3}1\}$	79°24′	1
$\{40\bar{4}1\}$	$83\pm2°$	18
$\{10\bar{1}0\}$	$90\pm2°$	5

The preceding results are based on a large number of measurements which included various checks on the self-consistency of the observations (Arnstein, 1970). It was found, for example, that the angular distance between equivalent reflections in a $\langle 1\bar{2}10\rangle$ type hole was 120°, as expected.

The optical goniometric measurements could not be made with sufficient precision to determine the manner in which particular faceted planes intersected each other along the directions forming the internal boundaries of the polygonal holes. In order to obtain information on this aspect of the sublimation structures, optical micrographs were taken with the optical axis approximately perpendicular to the inner boundary of the holes, *i.e.* nearly parallel to $\langle 1\bar{2}10\rangle$. Fig. 4 (*a*), (*b*), and (*c*) shows at increasing magnifications various sections of a boundary which defined the depths of a prominent hole that was examined in detail. The large density of parallel striae intersecting the segmented boundary mark the traces of the basal planes. The overall topographical features of this hole may be seen more clearly in the micrograph of Fig. 4 (*d*), which was obtained with the scanning electron microscope. The basal traces were used as reference directions to measure, say in the $\{1\bar{2}10\}$, projected angles that were made by the apparent boundary directions. Fig. 5 is a map of the projected traces of the various boundary directions relative to the horizontal $\{0001\}$ traces. In each case the boundary direction has itself been matched with a hypothetical direction corresponding to the intersection of two particular $\{h0\bar{h}l\}$ facet planes which are eligible to explain the intersected direction by virtue of the optical goniometric measurements. Table 3 presents all the information contained in Fig. 5, on the basis that the plane in which the measurements were made is $\{\bar{1}\bar{1}20\}$ and giving for comparison the calculated angles between these planes and directions.

Table 3. *Crystallographic analysis of a* $[\bar{1}\bar{1}20]$ *polygonal hole*

Planes in striated surface I	Planes in striated surface II	Directions of the sections of the boundary
$(0\bar{1}10)$	$(\bar{1}010)$	$[0001]$
$(0\bar{1}1\bar{1})$	$(\bar{1}011)$	$[1\bar{1}01]$
$(0\bar{1}11)$	$(\bar{1}01\bar{1})$	$[\bar{1}101]$
$(0\bar{2}2\bar{3})$	$(\bar{2}023)$	$[3\bar{3}02]$
$(0\bar{2}23)$	$(\bar{2}02\bar{3})$	$[\bar{3}302]$
$(0\bar{5}51)$	$(\bar{5}05\bar{1})$	$[\bar{1}105]$
$(0\bar{4}41)$	$(\bar{4}04\bar{1})$	$[\bar{1}104]$

The directions of intersection were calculated in two ways. First, under the assumption that only intersections of planes of the same family are to be expected – reasonable agreement with the observed directions was

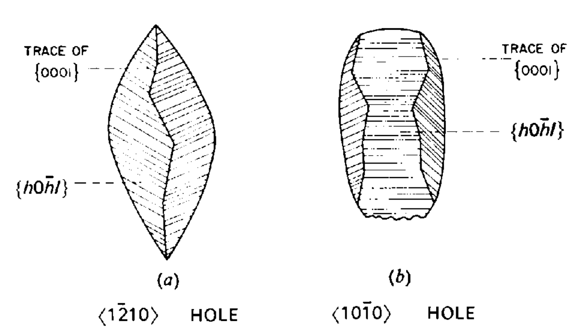

Fig. 3. Schematic diagram of the polygonal holes.

(a)

(b)

Fig. 2. Macroscopic views of a zinc single crystal partially sublimed at 370 °C.

[To face p. 346

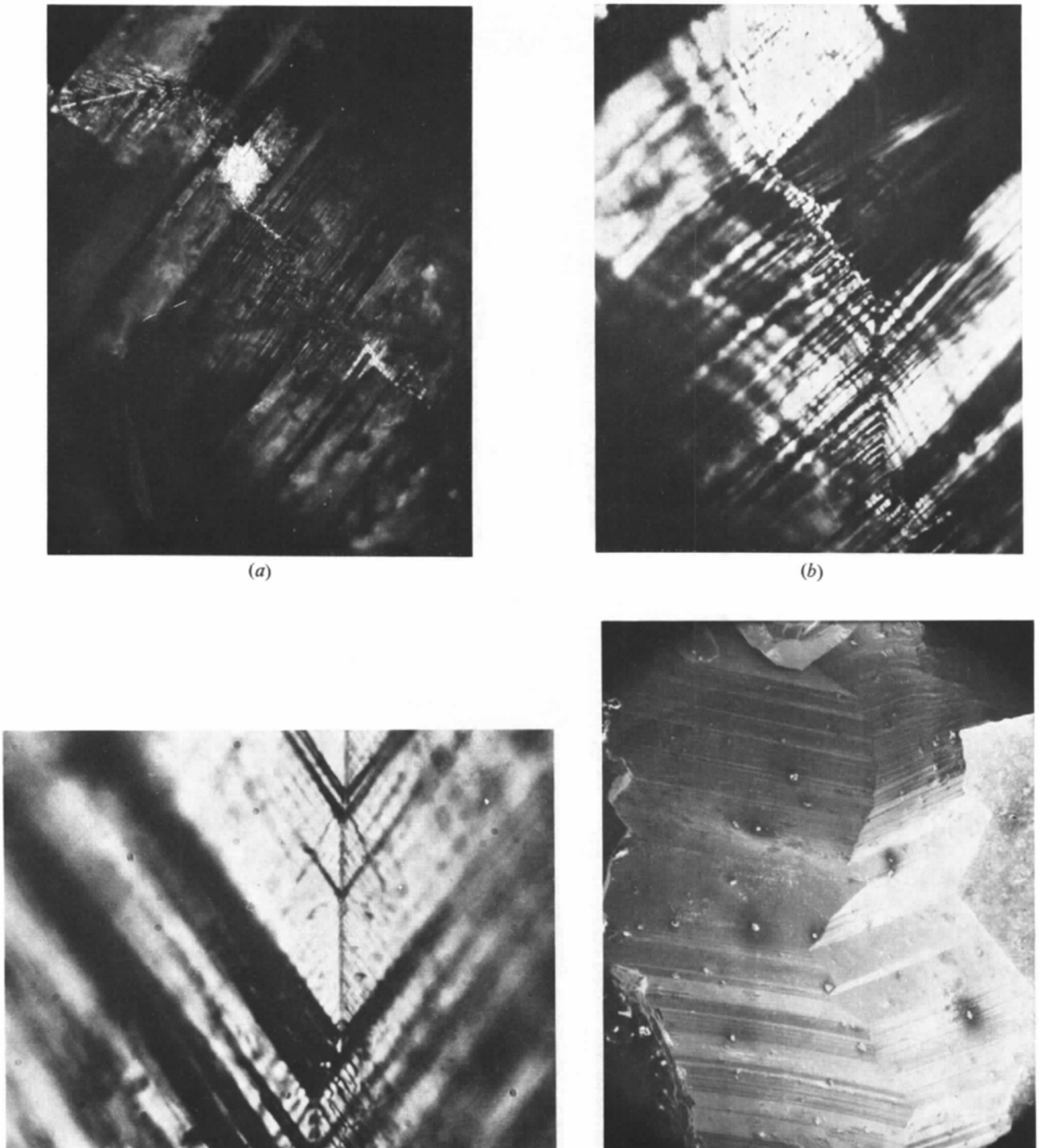

(a) (b)

(c) (d)

Fig. 4. Optical and electron scanning micrographs of a $\langle 1\bar{2}10\rangle$ polygonal hole: (a) $\times$ 50, (b) $\times$ 200, (c) $\times$ 560, (d) $\times$ 42 (electron scanning).

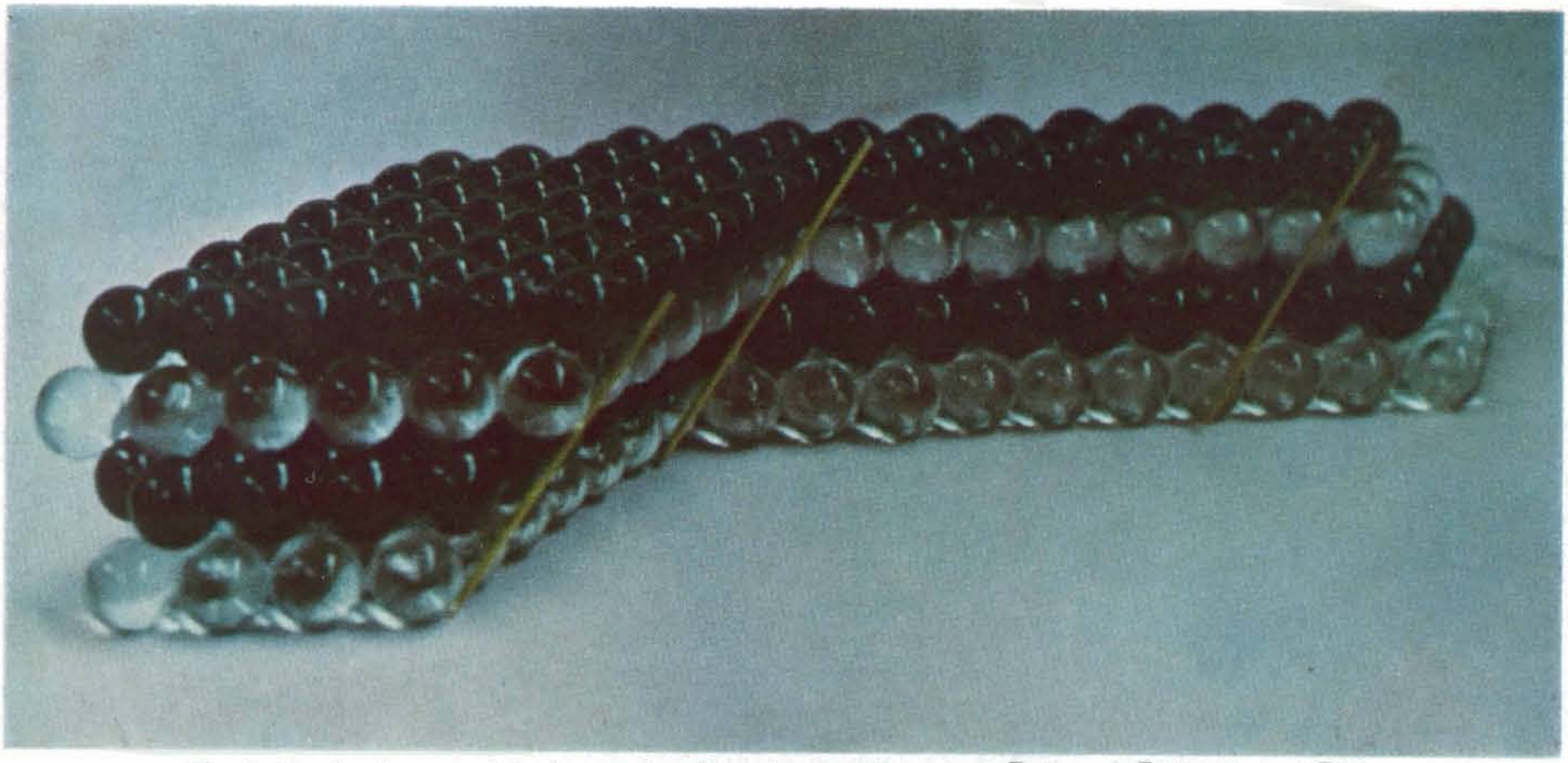

Fig. 7. Hard-sphere model of crystal surfaces intersection of a $(0\bar{1}11)$ and $(\bar{1}011)$ along $[1\bar{1}01]$.

Fig. 8. Hard-sphere model of crystal surface intersection of a $(0\bar{2}2\bar{3})$ and a $(\bar{2}023)$ along $[\bar{1}\bar{1}22]$.

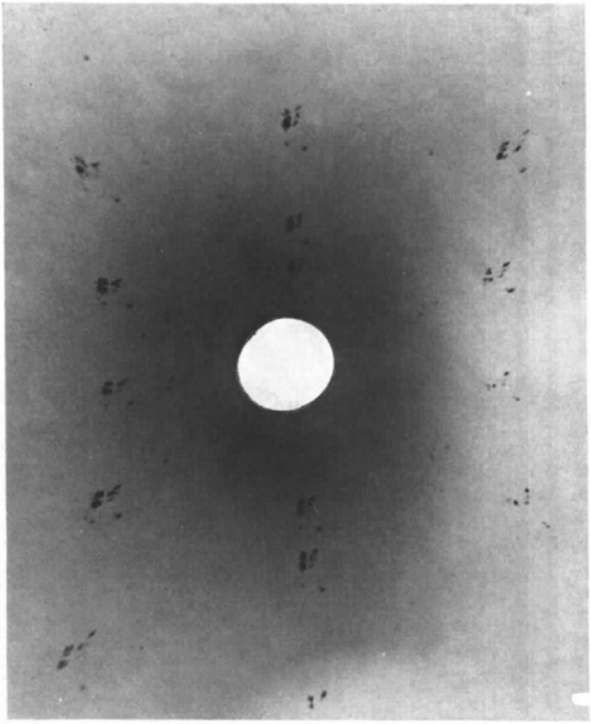

Fig. 12. Laue back-reflection pattern taken with the X-ray beam parallel to a $\langle 10\bar{1}0 \rangle$ polygonal hole.

obtained as is shown in Table 3. A second more general analysis involved placing all measured angles on a $(\bar{1}\bar{1}20)$ stereographic projection and comparing them with the angles between various combinations of the experimentally identified planes (Table 2) as computed by the equations given in the Appendix. This projection is shown in Fig. 6 where the open circles denote the measured angles.

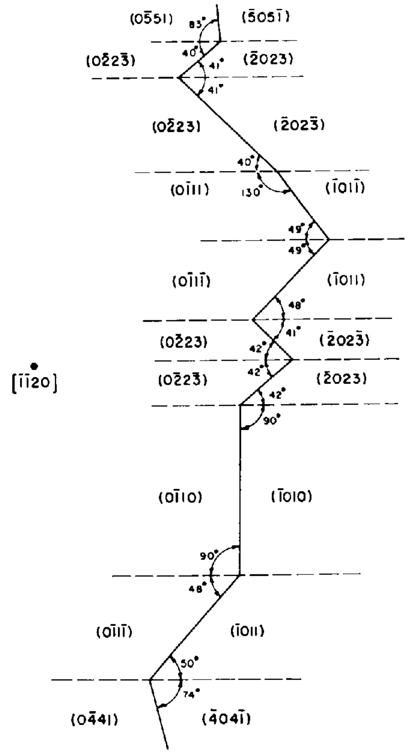

Fig. 5. Schematic diagram of angular relationship of the crystallographic surfaces of a section of hole shown in Fig. 4.

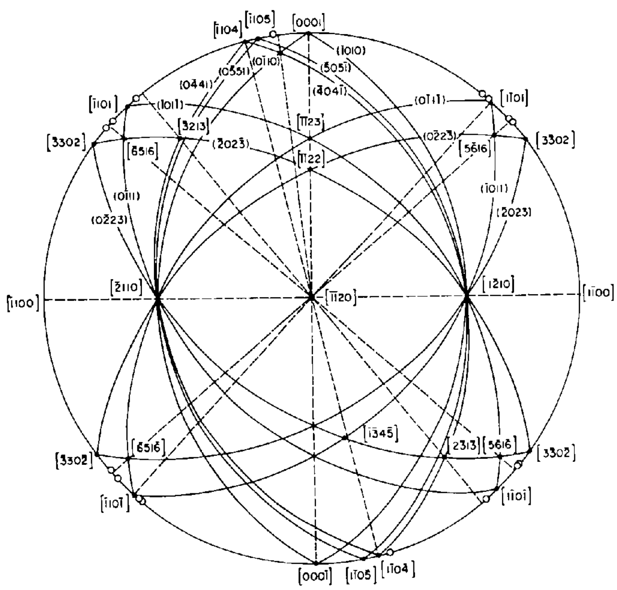

Fig. 6. Stereographic projection of planes and directions for analysis of plane intersections of $[\bar{1}\bar{1}20]$ sublimation in zinc.

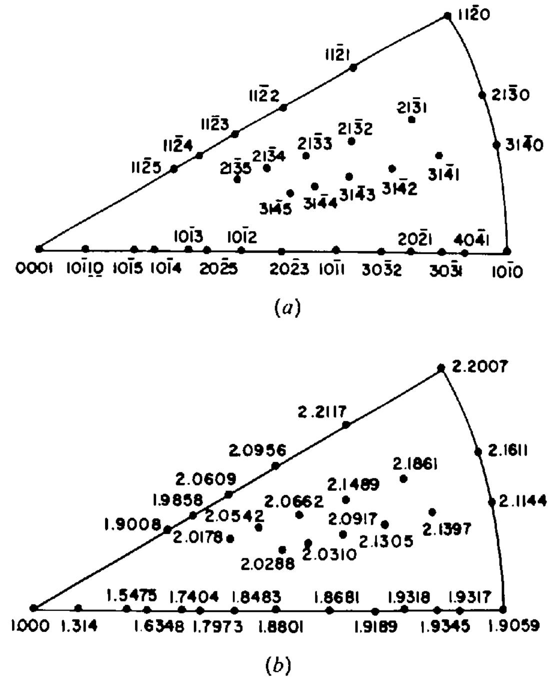

Fig. 9. (*a*) Stereographic projection of the planes in the (0001) $(10\bar{1}0)$ $(11\bar{2}0)$ triangle. (*b*) Stereographic representation of the relative surface free energy ($\gamma/\gamma(0001)$) of the planes in the (0001) $(10\bar{1}0)$ $(11\bar{2}0)$ triangle.

From this projection it is observed that some of the experimentally observed angles are better explained by the intersection of two planes from different families (*e.g.* the direction measurement attributed to the matching of an $(0\bar{1}1\bar{1})$ surface with a $(\bar{1}011)$ surface as shown in Fig. 5 appears closer to a $(0\bar{2}2\bar{3})$–$(\bar{1}011)$ matching in the stereographic projection). The fact that several of the observed angles correspond more closely to the matching of planes of different families of the $\{h0\bar{h}l\}$ type suggests that this is a systematic occurrence in the holes. These results were also confirmed by the construction of hard-sphere crystal models which demonstrate the configuration of different atomic-plane intersections (Nicholas, 1965), as shown in Figs. 7 and 8, where the matching of a $(\bar{1}011)$ surface with a $(0\bar{1}1\bar{1})$ surface and the matching of a $(0\bar{2}2\bar{3})$ surface with a $(\bar{2}023)$ surface are illustrated. Fig. 7 shows an example of the crystallographic nature of the diagonal section of the boundaries of the polygonal holes that give rise to the zigzag appearance of the total boundary which is seen in Figs. 4 and 5. Fig. 8 demonstrates that planes of type, say $\{20\bar{2}3\}$ may be viewed as being composed of segments of $\{0001\}$ and $\{10\bar{1}1\}$.

Discussion

The crystallographic indices which were determined for the planes exposed in the polygonal holes give, at first consideration, a qualitative indication that the anisotropy of the surface free energy of the h.c.p. lattice of zinc may play an important role in the macroscopic appearance of the partially sublimed crystals. This occurs because only $\{h0\bar{h}l\}$ surfaces were identified around the $\langle 0001 \rangle$ axis and these planes are of the same type as those composing the reported Gibbs–Wulff figure. Also, in agreement with Andrade & Randall (1950), it was observed that the basal surfaces of the crystals remained essentially inert during the sublimation process and this is consistent with the large anisotropy of the surface free energy of zinc.

The planes actually observed in our experiments are marked in Fig. 9 with respect to their orientation in the standard triangle and the computed (on the basis of pairwise interaction model) values of their surface free energies (Miller *et al.*, 1969; Wolff & Gualtieri, 1962). Fig. 9 shows that planes of type $\{h0\bar{h}l\}$ have the lowest surface free energies, which agrees with the observation made in the crystallographic holes. However, as can be seen in Fig. 10, planes of the type $\{40\bar{4}1\}$, $\{30\bar{3}1\}$, $\{30\bar{3}2\}$ and $\{20\bar{2}1\}$, which have been identified in the polygonal holes, are intermediate planes of higher energy separating planes of type $\{10\bar{1}1\}$ and $\{10\bar{1}0\}$. Similarly, the $\{20\bar{2}3\}$ and $\{40\bar{4}5\}$ are intermediate planes between the lower energy $\{10\bar{1}1\}$ and $\{0001\}$. Thus the presence in the polygonal holes of the intermediate surfaces of high relative energies is apparently inconsistent with the computed Gibbs–Wulff shape for zinc.

The appearance of planes other than $\{0001\}$, $\{10\bar{1}1\}$ and $\{10\bar{1}0\}$ implies that the macroscopic polygonal holes cannot be viewed as a simple aggregation of submicroscopic holes which do conform to the computed Gibbs–Wulff shape for zinc, barring the possibility that the computed Gibbs–Wulff shape itself is incorrect for the conditions of our experiment. It is possible that the model for the computed Gibbs–Wulff shape is incorrect or that preferential absorption of gaseous species has altered the relative stabilities of the various plane surfaces, as has been found to occur in f.c.c. materials (Gjostein, 1963; Blakely & Mykura, 1966).

Table 4. *Ratios for polygonal holes in zinc, height* (h) *to width* (w)

Hole	$\frac{h}{w}$	h (mm)
1	2·22	4
2	1·40	2·8
3	1·40	1·9
4	1·25	2·7
5	2·00	1·6
6	2·50	0·66
7	3·70	0·7
8	3·33	3·3
9	1·64	0·9
10	3·70	1·2
11	1·33	2·7
12	2·00	1·3

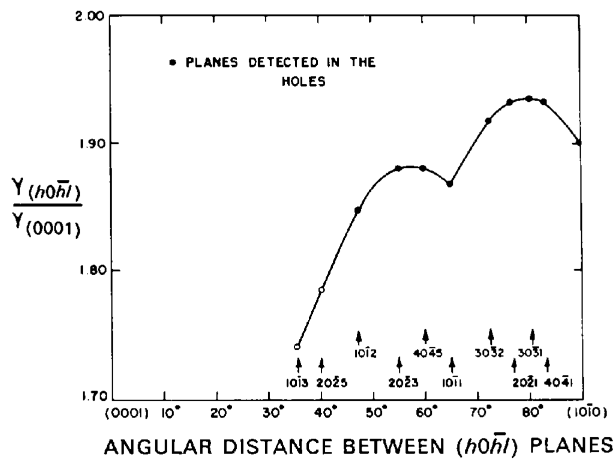

Fig. 10. (1$\bar{2}$10) partial section of the Gibbs–Wulff plot.

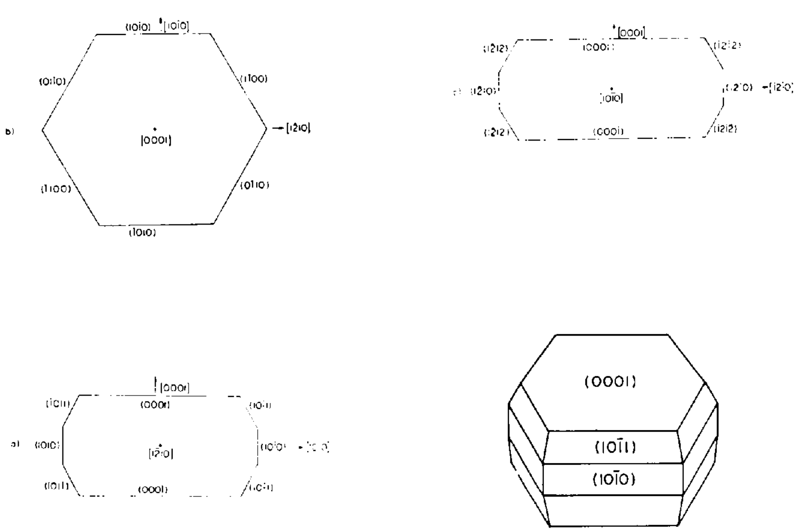

Fig. 11. Gibbs–Wulff construction for zinc as computed by Wolff & Gualtieri (1962).

The aspect ratio of the polygonal holes may also be compared with the Gibbs–Wulff shape predicted by the Gibbs–Wulff theorem (15, 16). In the case of zinc, the computed Gibbs–Wulff shape is a squat figure when viewed with the [0001] axis vertical. Along the $[\bar{1}\bar{1}20]$ the height (h) to width (w) ratio is 0·51 whereas along $[10\bar{1}0]$ the height to width ratio is 0·44. Fig. 11 shows these three two-dimensional views as they combine to form the computed three-dimensional Gibbs–Wulff shape. However, Figs. 2 and 4 (d) as well as the representative measured height to width ratio of holes listed in Table 4 contradict the aforementioned Gibbs–Wulff shape. The explanation for this phenomenon may lie in the enhanced nucleation of submicroscopic holes along a [0001] axis once an initial hole has formed, or by kinetic effects favoring the rapid growth of holes along the [0001] direction or, simply, by the inadequacy of the Gibbs–Wulff shape evaluated from the surface energies resulting from a pairwise interaction model.

A dislocation lineage structuie has been observed (Schultz & Armstrong, 1964) in our crystals following the crystal-solidification process. The dislocation subboundaries are oriented so that they contain the [0001] growth axis. The boundary misorientations appear to correspond mainly to tilts around axes in the {0001};

Table 5. *Angles between $\langle u_1v_1t_1w_1\rangle$ and $\langle u_2v_2t_2w_2\rangle$ for zinc* ($c/a = 1·8563$)

$[u_2v_2t_2w_2]$	$[u_1v_1t_1w_1]$ 0001	$1\bar{1}00$ / $01\bar{1}0$ / $\bar{1}010$	$2\bar{1}\bar{1}0$ / $\bar{1}2\bar{1}0$ / $\bar{1}\bar{1}20$
0001	0·000	90·000	90·000
		90·000	90·000
		90·000	90·000
$10\bar{1}0$	90·000	60·000	30·000
		60·000	90·000
		0·000	30·000
$10\bar{1}1$	43·016	70·055	53·785
		70·055	90·000
		46·983	53·785
$10\bar{1}2$	25·010	77·796	68·522
		77·796	90·000
		64·989	68·522
$10\bar{1}3$	17·276	81·460	75·096
		81·460	90·000
		72·723	75·096
$10\bar{1}4$	13·130	83·478	78·654
		83·478	90·000
		76·869	78·654
$10\bar{1}5$	10·570	84·737	80·858
		84·737	90·000
		79·429	80·858
$20\bar{2}1$	61·814	63·850	40·240
		63·850	90·000
		28·185	40·240
$20\bar{2}3$	31·883	74·686	62·778
		74·686	90·000
		58·116	62·778
$20\bar{2}5$	20·466	79·931	72·372
		79·931	90·000
		69·533	72·372
$30\bar{3}1$	70·341	61·910	35·358
		61·910	90·000
		19·659	35·358
$30\bar{3}2$	54·454	65·994	45·199
		65·994	90·000
		35·545	45·199
$40\bar{4}1$	75·000	61·120	33·225
		61·120	90·000
		14·999	33·225
$40\bar{4}3$	51·207	67·063	47·546
		67·063	90·000
		38·792	47·546
$40\bar{4}5$	36·739	72·597	58·799
		72·597	90·000
		53·260	58·799
$50\bar{5}1$	77·901	60·732	32·135
		60·732	90·000
		12·098	32·135

$[u_2v_2t_2w_2]$	$[u_1v_1t_1w_1]$ 0001	$1\bar{1}00$ / $01\bar{1}0$ / $\bar{1}010$	$2\bar{1}\bar{1}0$ / $\bar{1}2\bar{1}0$ / $\bar{1}\bar{1}20$
$11\bar{2}0$	90·000	90·000	60·000
		30·000	60·000
		30·000	0·000
$11\bar{2}1$	58·252	90·000	64·837
		42·570	64·837
		42·570	31·747
$11\bar{2}2$	38·940	90·000	71·684
		57·022	71·684
		57·022	51·059
$11\bar{2}3$	28·311	90·000	76·282
		65·749	76·282
		65·749	61·688
$11\bar{2}4$	22·000	90·000	79·204
		71·069	79·204
		71·069	67·999
$11\bar{2}5$	17·912	90·000	81·154
		74·552	81·154
		74·552	72·087
$21\bar{3}0$	90·000	79·106	49·106
		40·893	70·893
		19·106	10·893
$21\bar{3}1$	67·948	79·912	52·644
		45·522	72·339
		28·861	24·474
$21\bar{3}2$	50·987	81·556	59·424
		54·030	75·265
		42·760	40·270
$21\bar{3}3$	39·450	83·103	65·419
		61·293	77·995
		53·100	51·394
$21\bar{3}4$	31·681	84·303	69·890
		66·608	80·101
		60·246	58·953
$21\bar{3}5$	26·277	85·200	73·152
		70·448	81·667
		65·271	64·231
$31\bar{4}0$	90·000	73·897	43·897
		46·102	76·102
		13·897	16·102
$31\bar{4}1$	73·445	74·582	46·313
		48·345	76·689
		21·488	22·935
$31\bar{4}2$	59·268	76·207	51·728
		53·415	78·084
		33·445	34·324
$31\bar{4}3$	48·275	78·053	57·465
		58·835	79·672
		43·572	44·186

$[u_2v_2t_2w_2]$	$[u_1v_1t_1w_1]$ 0001	$1\bar{1}00$ / $01\bar{1}0$ / $\bar{1}010$	$2\bar{1}\bar{1}0$ / $\bar{1}2\bar{1}0$ / $\bar{1}\bar{1}20$
$31\bar{4}4$	40·065	79·716	62·366
		63·493	81·106
		51·330	51·799
$31\bar{4}5$	33·934	81·093	66·280
		67·227	82·294
		57·186	57·565
$31\bar{4}6$	29·279	82·020	69·365
		70·177	83·254
		61·656	61·973
$41\bar{5}0$	90·000	70·893	40·893
		49·106	79·106
		10·893	19·106
$41\bar{5}1$	76·836	71·414	42·602
		50·397	79·396
		17·024	23·061
$41\bar{5}2$	64·932	72·752	46·785
		53·630	80·143
		27·191	31·139
$41\bar{5}3$	54·945	74·457	51·770
		57·594	81·100
		36·499	39·329
$41\bar{5}4$	46·909	76·170	56·493
		61·440	82·067
		44·183	46·366
$41\bar{5}5$	40·536	77·717	60·574
		64·819	82·944
		50·341	52·111
$51\bar{6}0$	90·000	68·948	38·948
		51·051	81·051
		8·948	21·051
$51\bar{6}1$	79·104	69·345	40·209
		51·881	81·214
		14·064	23·589
$51\bar{6}2$	68·944	70·413	43·465
		54·080	81·653
		22·798	29·431
$51\bar{6}3$	59·995	71·876	47·663
		57·018	82·258
		31·191	36·081
$51\bar{6}4$	52·405	73·463	51·959
		60·126	82·920
		38·491	42·314
$51\bar{6}5$	46·096	75·000	55·920
		63·068	83·565
		44·623	47·746
$51\bar{6}6$	40·887	76·400	59·397
		65·702	84·156
		49·713	52·346

however, other rotation axes have also been observed (see *e.g.* Table 1). Because the orientation of the sub-boundary surfaces is predominantly parallel to ⟨0001⟩, we suggest that the elongated shape of the polygonal holes may in fact be determined by easy nucleation or growth of the holes along such boundaries. It was observed, as seen in Fig. 12, that the dislocation sub-boundary structure became sharply defined during the sublimation treatment but sufficiently precise measurements have not yet been made to assess the actual relation, if any, of the dislocation substructure to the sublimation structure. In this regard, it should be mentioned that the dislocation line orientations and Burgers vectors have also been described for crystals of the type employed in the present investigation (Schultz & Armstrong, 1964). The outstanding majority of dislocations lie in the basal plane. They appear to have line and Burgers vectors along $\langle 10\bar{1}0\rangle$ and $\langle 1\bar{2}10\rangle$. It also seems reasonable, therefore, that preferential sublimation should generally occur in directions orthogonal to [0001] as compared with the [0001] because the sublimation process occurs more easily at the emergence sites of the main quantity of dislocations.

Thermodynamically, the observation that sublimation takes place at distinct points on the crystal surface (*i.e.* to produce the polygonal holes) and that these

Table 6. *Angles between $\{h_1k_1i_1l_1\}$ and $\{h_2k_2i_2l_2\}$ for zinc* ($c/a = 1{\cdot}8563$)

$(n_2k_2i_2l_2)$	$(h_1k_1i_1l_1)$ 0001	$1\bar{1}00$ / $01\bar{1}0$ / $\bar{1}010$	$2\bar{1}\bar{1}0$ / $\bar{1}2\bar{1}0$ / $\bar{1}\bar{1}20$	$(h_2k_2i_2l_2)$	$(h_1k_1i_1l_1)$ 0001	$1\bar{1}00$ / $01\bar{1}0$ / $\bar{1}010$	$2\bar{1}\bar{1}0$ / $\bar{1}2\bar{1}0$ / $\bar{1}\bar{1}20$	$(h_2k_2i_2l_2)$	$(h_1k_1i_1l_1)$ 0001	$1\bar{1}00$ / $01\bar{1}0$ / $\bar{1}010$	$2\bar{1}\bar{1}0$ / $12\bar{1}0$ / $\bar{1}\bar{1}20$
0001	0·000	90·000	90·000	$11\bar{2}0$	90·000	90·000	60·000	$314\bar{4}$	62·635	75·740	50·212
		90·000	90·000			30·000	60·000			51·990	77·683
		90·000	90·000			30·000	60·000			30·446	31·432
$10\bar{1}0$	90·000	60·000	30·000	$11\bar{2}1$	74·952	90·000	61·132	$314\bar{5}$	57·098	76·534	52·771
		60·000	90·000			33·256	61·132			54·397	78·365
		0·000	30·000			33·256	15·074			35·409	36·228
$10\bar{1}1$	64·989	63·056	38·296	$11\bar{2}2$	61·688	90·000	63·883	$314\bar{6}$	52·176	77·345	55·306
		63·056	90·000			40·320	63·883			56·790	79·063
		25·010	38·296			40·320	28·311			39·934	40·631
$10\bar{1}2$	46·983	68·556	50·713	$11\bar{2}3$	51·060	90·000	67·113	$41\bar{5}0$	90·000	70·893	40·893
		68·556	90·000			47·654	67·113			49·106	79·106
		43·016	50·713			47·654	38·939			10·893	19·106
$10\bar{1}3$	35·545	73·101	59·770	$11\bar{2}4$	42·866	90·000	70·114	$41\bar{5}1$	84·187	70·995	41·232
		73·101	90·000			53·903	70·114			49·361	79·163
		54·454	59·770			53·903	47·133			12·330	19·939
$10\bar{1}4$	28·185	76·339	65·854	$11\bar{2}5$	36·594	90·000	72·657	$41\bar{5}2$	78·491	71·292	42·206
		76·339	90·000			58·916	72·657			50·096	79·328
		61·814	65·854			58·916	53·405			15·795	22·193
$10\bar{1}5$	23·204	78·637	70·048	$21\bar{3}0$	90·000	79·106	49·106	$41\bar{5}3$	73·016	71·756	43·700
		78·637	90·000			40·893	70·893			51·236	79·587
		66·795	70·048			19·106	10·893			20·089	25·350
$20\bar{2}1$	76·869	60·861	32·500	$21\bar{3}1$	79·999	79·274	49·856	$41\bar{5}4$	67·842	72·352	45·564
		60·861	90·000			41·888	71·194			52·676	79·919
		13·130	32·500			21·478	14·746			24·568	28·939
$20\bar{2}3$	55·016	65·816	44·802	$21\bar{3}2$	70·574	79·733	51·874	$41\bar{5}5$	63·022	73·039	47·648
		65·816	90·000			44·529	72·019			54·308	80·304
		34·984	44·802			26·985	22·168			28·939	32·638
$20\bar{2}5$	40·609	71·007	55·688	$21\bar{3}3$	62·121	80·383	54·642	$51\bar{6}0$	90·000	68·948	38·948
		71·007	90·000			48·072	73·181			51·051	81·051
		49·390	55·688			33·358	29·771			8·948	21·051
$30\bar{3}1$	81·160	60·392	31·158	$21\bar{3}4$	54·803	81·116	57·658	$51\bar{6}1$	85·210	69·025	39·195
		60·392	90·000			51·849	74·485			51·213	81·083
		8·839	31·158			39·451	36·634			10·140	21·565
$30\bar{3}2$	72·723	61·481	34·213	$21\bar{3}5$	48·598	81·850	60·590	$51\bar{6}2$	80·486	69·251	39·913
		61·481	90·000			55·457	75·787			51·685	81·175
		17·276	34·213			44·864	42·559			13·032	23·012
$40\bar{4}1$	83·347	60·222	30·661	$31\bar{4}0$	90·000	73·897	43·897	$51\bar{6}3$	75·889	69·612	41·040
		60·222	90·000			46·102	76·102			52·435	81·323
		6·652	30·661			13·897	16·102			16·659	25·163
$40\bar{4}3$	70·715	61·839	35·171	$31\bar{4}1$	82·627	74·034	44·388	$51\bar{6}4$	71·470	70·087	42·489
		61·839	90·000			46·556	76·219			53·413	81·719
		19·284	35·171			15·698	17·669			20·508	27·763
$40\bar{4}5$	59·751	64·410	41·573	$31\bar{4}2$	75·491	74·424	45·765	$51\bar{6}5$	67·268	70·651	44·167
		64·410	90·000			47·835	76·553			54·564	81·651
		30·249	41·573			19·987	21·545			24·342	30·597
$50\bar{5}1$	84·669	60·143	30·426	$31\bar{4}3$	68·785	75·015	47·798	$51\bar{6}6$	63·309	71·280	45·985
		60·143	90·000			49·730	77·061			55·831	82·011
		5·330	30·426			25·185	26·407			28·046	33·507

polygonal holes have a definite preferred orientation with respect to the crystal axes suggests that their formation may be primarily controlled by a nucleation type process. Furthermore, since the walls of the polygonal holes consist primarily of the planes figuring in the Gibbs–Wulff plot, we may assume that the polygonal holes are in fact composite sections of the three

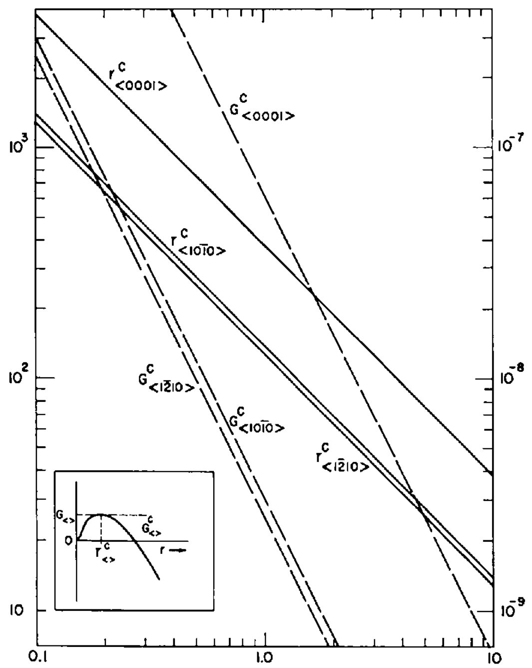

Fig. 13. Critical hole size as a function of superheating.

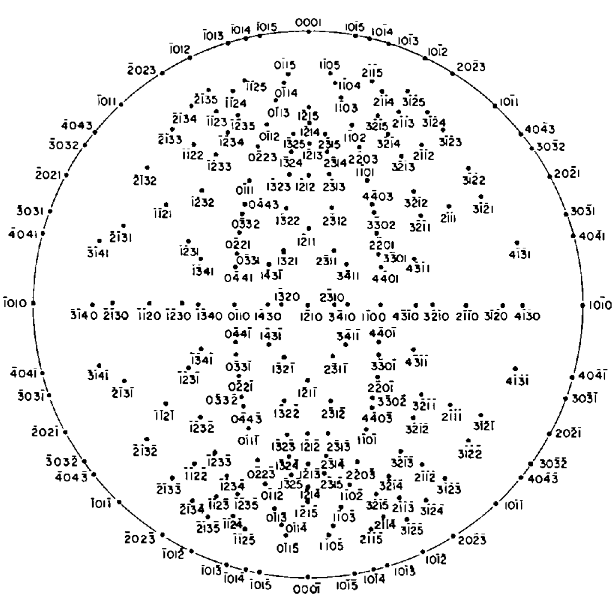
Fig. 14. [$1\bar{2}10$] standard projection for zinc ($c/a = 1{\cdot}8563$).

dimensional plot shown in Fig. 11 with the basal plane surface decomposed into terrace-like steps. The fact that the macroscopic shape of the holes does not conform to that of the Gibbs–Wulff construction, as we said before, may be due to the inadequacy of the pairwise model used to calculate the surface free energies or to the hole growth kinetics. Assuming for the present that the latter is the cause of the shape discrepancy, but without loss of generality, one can describe the formation of polygonal holes by conventional nucleation theory.

Sections through the center of the Gibbs–Wulff shape (Fig. 11) and parallel, in turn, to $\{10\bar{1}0\}$, $\{1\bar{2}10\}$ and $\{0001\}$ would produce polygonal holes of the $\langle 10\bar{1}0\rangle$, $\langle 1\bar{2}10\rangle$ and $\langle 0001\rangle$ types respectively. The $\langle 0001\rangle$ type, although not observed experimentally, is included to give a measure of the relative stability of the various types of holes. The total energy required to form a polygonal hole of dimension, r, of each of the aforementioned types is:

$$G\langle 10\bar{1}0\rangle = \tfrac{1}{2}r^3V\Delta G_V + \tfrac{1}{2}r^2[A\{10\bar{1}0\}\gamma\{10\bar{1}0\} + A\{1\bar{2}10\}\gamma\{1\bar{2}10\} + A\{0001\}\gamma\{0001\}] - r^2A^*\{10\bar{1}0\}\gamma\{10\bar{1}0\}\,,$$

or,

$$G\langle 10\bar{1}0\rangle = \tfrac{1}{2}r^3V\Delta G_V + \tfrac{1}{2}r^2\Delta G_A - r^2A^*\{10\bar{1}0\}\gamma\{10\bar{1}0\};$$
$$G\langle 1\bar{2}10\rangle = \tfrac{1}{2}r^3V\Delta G_V + \tfrac{1}{2}r^2\Delta G_A - r^2A^{**}\{1\bar{2}10\}\gamma\{1\bar{2}10\};$$

and,

$$G\langle 0001\rangle = \tfrac{1}{2}r^3V\Delta G_V + \tfrac{1}{2}r^2\Delta G_A - r^2A^{***}\{0001\}\gamma\{0001\}\,,$$

where r is the distance from the center of the three-dimensional γ plot to the (0001) surface; r^3V is the volume of the three-dimensional γ plot; and ΔG_V is the volumetric free energy of sublimation; r^2A is the total area of each type of surface; $\gamma\{hkil\}$ is the surface free energy; and r^2A^*, r^2A^{**} and r^2A^{***} are the areas of the plane disappearing upon formation of a polygonal hole in each case considered. The numerical values of these quantities can be derived on the basis of the angular relations given in the Appendix and the estimated values of the relative surface energies of various planes (Miller *et al.*, 1969; Wolff & Gualtieri, 1962).

Now, if a crystal is held in an atmosphere having a partial pressure of zinc lower than the equilibrium vapor pressure at the temperature, T, in question, there is a net overheating of the crystal which amounts to an energy decrease on sublimation given by:

$$\Delta G_V = RT \ln\,[P^0_{\mathrm{Zn},T}/P^0_{\mathrm{Zn},T_s}]$$

where T_s is the temperature corresponding to equilibrium for the partial pressure of zinc in the atmosphere in question. On the basis of the above equations one can calculate the size of a critical polygonal hole by setting $(\partial G\langle uvzw\rangle/\partial r)_{r_c} = 0$. The results of such calculations of critical size *versus* degree of superheating for $T = 350\,°\mathrm{C}$ and $\gamma\{0001\} = 600$ erg.cm^{-2} (Miller *et al.*, 1969) are shown in Fig. 13.

A quantitative evaluation of the obtained experimental results on this basis is, of course, not possible because of the unknown effective T_s, the exact configuration of active sites in terms of dislocations and subgrain boundaries, and the lack of information on the growth kinetics after the polygonal holes are nucleated. The results do confirm the strong anisotropy which is expected for the sublimation process. The fact that the basal plane remains essentially unmarked by polygonal holes and the $\langle 10\bar{1}0\rangle$ and $\langle 1\bar{2}10\rangle$ holes appear with nearly the same frequency is borne out by this calculation. This effect should be further enhanced by the orientation of dislocations discussed previously.

The preceding calculation also gives an indication of the nature of the transition from a thermal etching to a thermal faceting process (Moore, 1963). Although thermal etching and thermal faceting may actually be different in principle, they share a common feature in that when a solid is heated in high vacuum or in an atmosphere under which appreciable sublimation occurs (thermal etching) or in some near equilibrium atmosphere (thermal faceting) for a period of time, the surface of the solid shows preferential sites of transformation containing definite crystallographic planes, usually ones of high atomic density. Thermal faceting may be regarded as thermal etching in the limit of $T-T_s=\Delta T\rightarrow 0$ and, since in this limit the critical size of the polygonal hole approaches that of the sample itself, faceting should be observable only when the crystal size is very small (Herring, 1951) or in small regions of a crystal where local temperature fluctuations are sufficiently large to nucleate some equilibrium facets. Such nucleation of small facets has been observed in copper (Mykura, 1969), suggesting that sublimation at very small superheatings and under closely controlled conditions may provide a useful method for the study of the anisotropy of surface energy in crystalline solids.

Conclusions

(1) The partial sublimation of [0001] zinc single crystals produces polygonal holes in directions orthogonal to [0001]. The holes are composed entirely of $\{h0\bar{h}l\}$ planes of which some types are clearly identified and other types are only probably detected.

(2) The Gibbs–Wulff shape evaluated by a pairwise interaction model is not in agreement with all of the plane surfaces which were identified nor with the macroscopic shape of the polygonal holes, except for the general fact that the relatively low energy surfaces $\{h0\bar{h}l\}$ as compared with $\{hkil\}$ are found to bound the holes. The shape of the holes suggests that the relative energy of the $\{h0\bar{h}l\}$ planes may be lower than calculated by the aforementioned model.

(3) The crystallographic orientation of the boundaries produced by intersecting facets and the striated surfaces of the polygonal holes seems to indicate that the shape and the position of the polygonal holes are related to the dislocation substructure of the material. The dislocation substructure was altered during the sublimation process as was observed in Laue back-reflection pictures taken of the crystals before and after the sublimation treatments.

(4) The frequency of appearance of different types of polygonal holes is in qualitative agreement with a conventional nucleation analysis. This orientation dependence is in agreement with the results expected on the basis of the character and the configuration of dislocations in the crystals.

The authors thank Dr A. W. Ruff Jr of the National Bureau of Standards and Mr J. V. Larsen of the Naval Ordnance Laboratory for making available certain facilities.

This research has been supported by the Advanced Projects Agency of the U.S. Government through the Center of Materials Research of The University of Maryland. GMA was financially supported by a fellowship sponsored jointly by the Council of Scientific and Humanistic Development of the Central University of Venezuela (UCV) and the Creole Foundation.

APPENDIX

The $[\bar{1}\bar{1}20]$ standard projection and the $(\bar{1}\bar{1}20)$ standard projection for zinc ($c/a=1\cdot8563$) were constructed after the angles between $\langle\bar{1}\bar{1}20\rangle$ and $\langle u_2v_2t_2w_2\rangle$ and the angles between $\{\bar{1}\bar{1}20\}$ and $\{h_2k_2i_2l_2\}$ were computed, using for directions

$$\cos\beta=\frac{u_1u_2+v_1v_2+\frac{1}{2}(u_1v_2+u_2v_1)+\frac{1}{3}w_1w_2(c/a)^2}{[u_1^2+v_1^2+u_1v_1+\frac{1}{3}w_1^2(c/a)^2]^{1/2}[u_2^2+v_2^2+u_2v_2+\frac{1}{3}w^2(c/a)^2]^{1/2}}$$

and for planes

$$\cos\alpha=\frac{h_1h_2+k_1k_2+\frac{1}{2}(h_1k_1+h_2k_1)+\frac{3}{4}l_1l_2(a/c)^2}{[h_1^2+k_1^2+h_1k_2+\frac{3}{4}l_1^2(a/c)^2]^{1/2}[h_2^2+k_2^2+h_2k_2+\frac{3}{4}l_2^2(a/c)^2]^{1/2}}\;.$$

These formulas were derived by vector analysis (Arnstein, 1970). Tables 5 and 6 present the angles calculated for both cases. Figs. 14 and 15 show the standard projections which result. Additional computed angles between $\langle 0001\rangle$ or $\langle 10\bar{1}0\rangle$ and other directions and between $\{0001\}$ or $\{10\bar{1}0\}$ and other planes are also given in these Tables. The angles between directions can also be calculated by employing the third index t, in which case the crystal symmetry is more clearly recognized and the possibility of misapplying the formulae by taking u and v to be defined for incorrect axes is avoided; *e.g.*

$$\cos\beta=\frac{u_1u_2+v_1v_2+t_1t_2+\frac{1}{2}(u_1v_2+u_2v_1+u_1t_2+u_2t_1+v_1t_2+v_2t_1)+\frac{1}{3}w_1w_2(c/a)^2}{[u_1^2+v_1^2+t_1^2+u_1v_1+u_1t_1+v_1t_1+\frac{1}{3}w_1^2(c/a)^2]^{1/2}[u_2^2+v_2^2+t_2^2+u_2v_2+u_2t_2+v_2t_2+\frac{1}{3}w_2^2(c/a)^2]^{1/2}}\,.$$

Pertinent references for this Appendix are Govila (1969), Lawley (1960), Metzbower (1969), Nicholas (1966, 1970), Salkovitz (1951), Taylor & Leber (1954).

References

ANDRADE, E. N. DA C. & RANDALL, R. F. Y. (1950). *Proc. Phys. Soc.* B**63**, 198.

ARNSTEIN, G. M. (1970). M.Sc. Thesis, Univ. of Maryland.

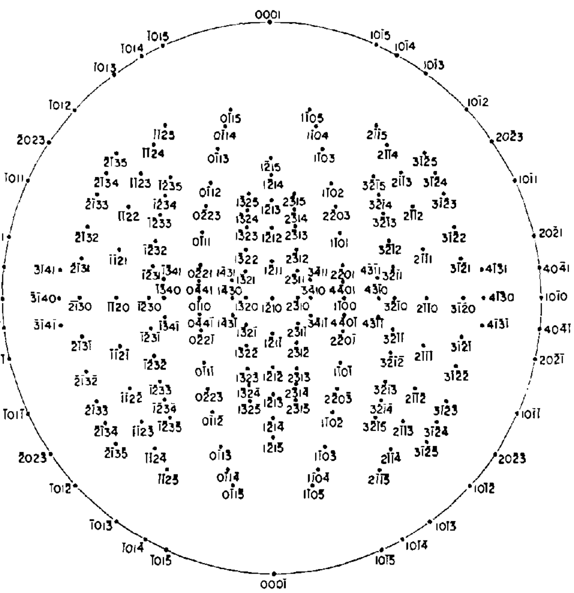

Fig. 15. ($1\bar{2}10$) standard projection for zinc $(c/a)=1{\cdot}8563$).

BLAKELY, J. M. & MYKURA, H. (1966). *Acta Metall.* **9**, 595

DARKEN, L. S. & GURRY, R. W. (1953). *Physical Chemistry of Metals*, p. 349. New York: McGraw-Hill.

DRECHSLER, M. & NICHOLAS, J. F. (1967). *J. Phys. Chem. Solids*, **28**, 2609.

GIBBS, J. W. (1961). *The Scientific Papers of J. Willard Gibbs*, Vol. 1 (*Thermodynamics*), p. 55. New York: Dover.

GJOSTEIN, N. A. (1963). *Acta Metall.* **11**, 969.

GOVILA, R. K. (1969). *TMS Paper Selection*, No. A69–12. The Metallurgical Society of AIME.

HERRING, C. (1951). *Phys. Rev.* **82**, 87.

KIRCHNER, H. O. K. & CHADWICK, G. A. (1969). *Phil. Mag.* **20**, 406.

LAWLEY, A. (1960). *Trans. TMS-AIME*, **218**, 957.

METZBOWER, E. A. (1969). NRL Report 6919, Naval Research Laboratory, Washington, D.C.

MILLER, W. A., CARPENTER, G. J. C. & CHADWICK, G. A. (1969). *Phil. Mag.* **20**, 406.

MOORE, A. J. W. (1958). *Acta Metall.* **6**, 293.

MOORE, A. J. W. (1963). *Metal Surfaces: Structure, Energetics and Kinetics*, p. 155. Cleveland: ASM.

MYKURA, H. (1969). *Molecular Processes on Solid Surfaces*, p. 129. New York: McGraw-Hill.

NICHOLAS, J. F. (1965). *An Atlas of Models of Crystal Surfaces*. New York: Gordon and Breach.

NICHOLAS, J. F. (1966). *Acta Cryst.* **21**, 880.

NICHOLAS, J. F. (1970). *Phys. Stat. Sol.* (*a*) **1**, 563.

SALKOVITZ, E. I. (1951). *Trans. TMS-AIME*, **191**, 64.

SCHULTZ, J. M. & ARMSTRONG, R. W. (1964). *Phil. Mag.* **10**, 497.

TAYLOR, A. & LEBER, S. (1954). *Trans. TMS-AIME*, **200**, 190.

WOLFF, G. A. & GUALTIERI, J. G. (1962). *Amer. Miner.* **47**, 562.

WULFF, G. (1901). *Z. Kristallogr.* **34**, 449.

Acta Cryst. (1972). A**28**, 353

On a New Retigraph with Pure Precession Motion

BY GLAUCO GOTTARDI

Istituto di Mineralogia e Petrologia, Università di Modena, Italy

(*Received* 21 *January* 1972)

A new precession retigraph is described which allows precession angles of up to 45°. It does not contain a universal-joint suspension, and it has a pure precession motion.

Introduction

An instrument capable of giving an undistorted photograph of the reciprocal lattice is usually called a 'retigraph'. All retigraphs are characterized by the presence of a crystal support and a film support, both of which must have exactly the same movement. One can identify three classes of instruments depending on the kind of movement: rotation models, precession models and generalized-movement models. The retigraphs of the different classes give spots of different shapes, and different Lorentz factors must be used in correcting the intensities.

The first retigraph was built by de Jong & Bouman